Applied Mathematical Modelling 121 (2023) 96–110

Contents lists available at ScienceDirect

Applied Mathematical Modelling

journal homepage: www.elsevier.com/locate/apm

# Mathematical modelling of haemorrhagic transformation in the human brain

Xi Chen[a,1], Jiayu Wang[a,1,*], Katinka R. van Kranendonk[b], Tamas.I. Józsa[a,b], Wahbi K. El-Bouri[c,d], Manon Kappelhof[b], Matthijs van der Sluijs[e], Diederik Dippel[f], Yvo B.W.M. Roos[g], Henk A Marquering[b,h], Charles B.L.M. Majoie[b], Stephen J. Payne[i]

[a] *Institute of Biomedical Engineering, Department of Engineering Science, University of Oxford, Oxford, UK*
[b] *Department of Radiology and Nuclear Medicine, Amsterdam University Medical Centers, location, Amsterdam Neurosciences, University of Amsterdam, Amsterdam, the Netherlands*
[c] *Liverpool Centre for Cardiovascular Science, University of Liverpool and Liverpool Heart & Chest Hospital Liverpool, UK*
[d] *Department of Cardiovascular and Metabolic Medicine, University of Liverpool, UK*
[e] *Department of Radiology & Nuclear Medicine, Erasmus MC-University Medical Center Rotterdam, Rotterdam, the Netherlands*
[f] *Department of Neurology, Erasmus MC-University Medical Center Rotterdam, Rotterdam, the Netherlands*
[g] *Department of Neurology, Amsterdam UMC, Location AMC, University of Amsterdam, Amsterdam, the Netherlands*
[h] *Department of Biomedical Engineering and Physics, Amsterdam UMC, Location AMC, University of Amsterdam, Amsterdam, the Netherlands*
[i] *Institute of Applied Mechanics, National Taiwan University, Taiwan*

ARTICLE INFO

*Article history:*
Received 13 December 2022
Revised 18 April 2023
Accepted 25 April 2023
Available online 28 April 2023

*Keywords:*
Haemorrhagic transformation
Ischaemic stroke
Cerebral blood flow
Finite element method

ABSTRACT

*Objective:* Haemorrhagic transformation (HT) is one of the most common complications after ischaemic stroke. HT can be the result of stroke progression or a complication of reperfusion treatment for stroke. The aim of this study is to apply a previously proposed HT mathematical model within a computational whole brain model to determine the factors that affect the severity of HT. In addition, these simulations are directly compared with neuroimaging data.

*Approach:* The MR CLEAN–NO IV trial assessed the effect of endovascular therapy (EVT) alone compared with intravenous alteplase treatment (IVT) followed by EVT for patients with acute ischaemic stroke due to anterior circulation large vessel occlusion. We included imaging data of 15 HT patients from the MR CLEAN–NO IV trial, 5 patients suffered from haemorrhagic infarction type 1, 5 from haemorrhagic infarction type 2 and 5 had parenchymal haematoma type 1. The comparison of simulations with patient image data is carried out by comparing the haematoma locations and haematoma volume. The parameters of the model are then optimised to improve agreement with clinical data. Finally, the model is used to investigate the factors that affect the severity of HT.

*Main results:* Based on the computational whole brain model, we found that perfusion reduced by 5–16% after HT onset. The results are in good agreement with the clinical data. We then showed that 1% increase of blood viscosity reduces perfusion by 0.04% and in-

* Corresponding author.
*E-mail address:* Jiayu.wang@eng.ox.ac.uk (J. Wang).
[1] These authors contributed equally to this work.

https://doi.org/10.1016/j.apm.2023.04.031

creases haematoma volume by 10.35% from baseline, and 1% increase of blood pressure reduces perfusion by 0.80% and increases haematoma volume by 4.73% from baseline. These results indicate that increased blood glucose and hypertension (among other factors) both appear to lead to a higher severity of HT.
*Significance:* This model, by enabling us to bridge the gap between the mathematical HT model and clinical imaging data, provides the first whole brain prediction model for HT severity assessment.



## 1. Introduction

Stroke is one of the most important causes of damage to the brain and was ranked as the second leading cause of death across the world in 2018 [1]. The incidence of stroke is predicted to continue to increase in ageing populations. Haemorrhagic transformation (HT) is one of the most common complications after ischaemic stroke, caused by damage to the blood–brain barrier (BBB) that can be the result of stroke progression or a complication of stroke treatment with reperfusion therapy. HT is a frequent, often asymptomatic, complication [2] that potentially leads to long-term morbidity and mortality [3].

The Heidelberg Bleeding classification which incorporates the European Cooperative Acute Stroke Study (ECASS) classification, classifies HT based on its radiological appearance on follow-up computed tomography (CT) or magnetic resonance imaging (MRI) [4]: haemorrhagic infarction type 1 (HI1), is defined as small petechiae (tiny spots of bleeding) along the peripheral margins of infarct; haemorrhagic infarction type 2 (HI2) as confluent petechiae within the infarcted area but without mass effect; parenchymal haematoma type 1 (PH1), as blood clots in $\leq$ 30% of the infarcted area with some slight mass effect; and parenchymal haematoma type 2 (PH2) as blood clots in $>$ 30% of the infarcted area with substantial mass effect. HT can also be quantified by measuring its volume and large volumes have been found to be associated with poor functional outcomes [5]. HT is often located in the internal regions of the brain: putamen (occurrence: 46.2%), thalamus (occurrence: 19.4%) and pons (occurrence: 14%) [6].

The severity of HT is highly variable. A key question is whether the occurrence and severity of HT can be predicted accurately after ischaemic stroke, based on available imaging data and clinical parameters. Wang and Payne [7] first proposed a mathematical model that describes the behaviour of HT within a 2D vasculature model. In this vasculature model, the geometries of vessels in the same generation were the same. However, based on anatomical studies, capillaries have been shown to have a more web-like than tree-like structure [8]. In addition, the effects of HT on surrounding normal vessels and tissue were not considered in this initial model.

Wang et al. [9] extended the previous model to an enlarged vasculature length scale in order to compare the model predictions more accurately with the human vasculature. The penetrating model they used was that of El-Bouri and Payne [10] and they investigated the effects of HT on the surrounding tissue and vessels. It was found that perfusion reduces by approximately $13-17\%$ and cerebral blood volume (CBV) reduces by around $20-25\%$ after HT onset due to the effect of capillary compression caused by increased interstitial pressure (the perfusion reduction was assumed to be fully caused by HT). However, this model focuses on a length scale of around 1mm, which remains difficult to compare with imaging data.

Therefore, it is necessary to extend the HT model to a full brain length scale (100mm) and validate this model with real imaging data, as shown in Fig. 1. Various full brain models have been developed, for example, to investigate the correlation between stress and midline shift (MLS) [11], to study the importance of different constitutive relationships and material properties [12], to explore the risk factors associated with the early stages of Alzheimer's disease [13] and to simulate tissue perfusion [14]. However, a full brain model that describes HT has not previously been developed.

The aim of this study is thus to develop a model that can simulate the severity of haemorrhage in a full brain model. In addition, this model has the potential to be used to help clinicians to determine the bleeding region more accurately for detecting small HT (volume $<$ 5ml). We used the HT model developed by Wang and Payne [7] and Wang et al. [9], which we further extended by inclusion of an oedema model developed by Mokhtarudin and Payne [15] and Chen et al. [16].

The developed HT model is applied to provide information in addition to a perfusion model described by Guo et al. [13], Padmos et al. [14] and Józsa et al. [17]. Then our results are compared with imaging data from the MR CLEAN–NO IV trial [18]. Properties such as haematoma volume are estimated and compared with neuroimaging measurements [18,19]. By comparing with the clinical data, the parameters used for our simulations, such as the definition of haematoma surface pressure, can be optimised. We then conclude by investigating the factors that may affect the severity of HT, including increased blood viscosity and blood pressure.

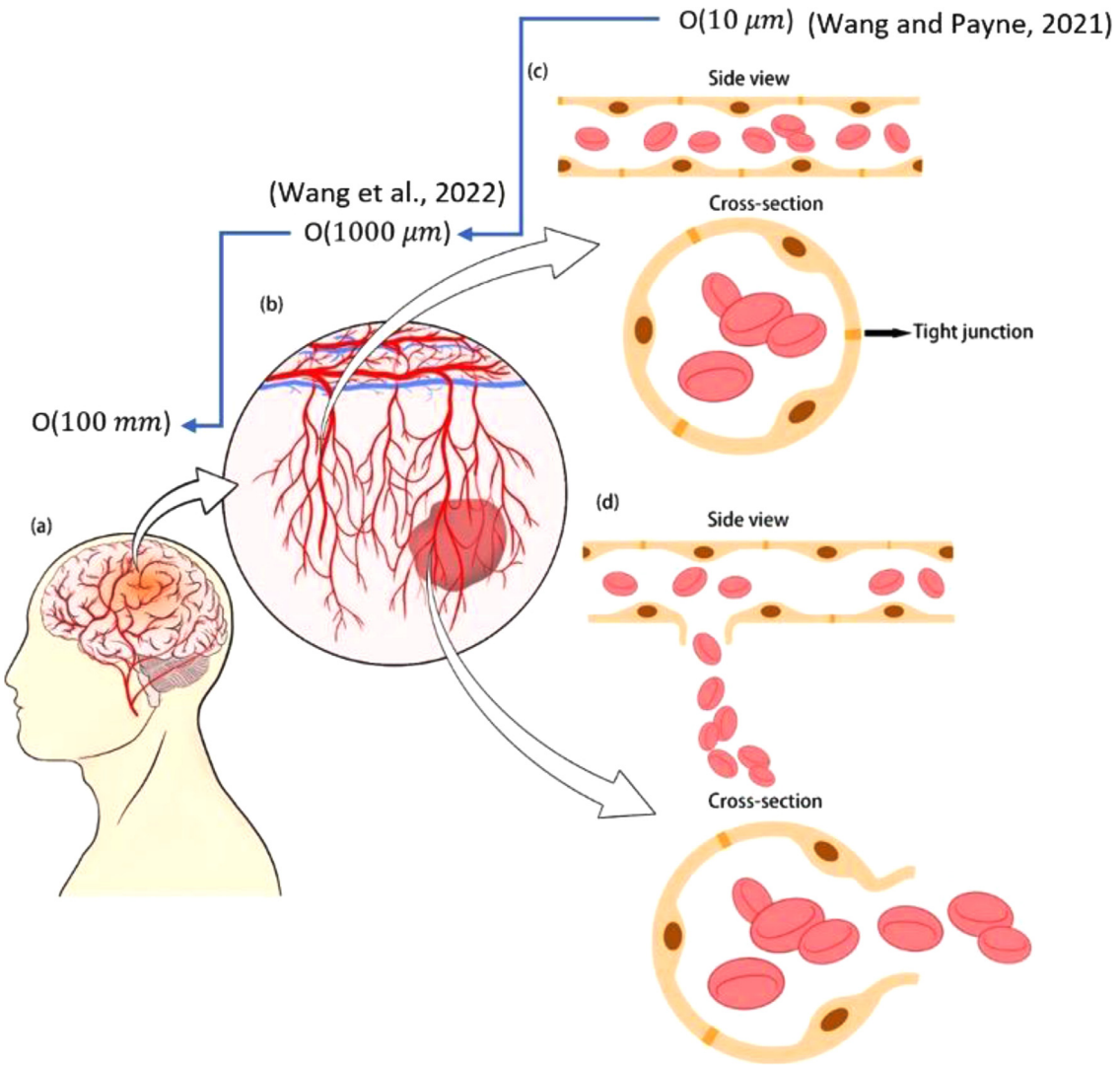


**Fig. 1.** Macroscopic (a) and microscopic (b, c, d) configurations of haemorrhagic transformation (HT) simulation across different length: (a) HT model in the entire human brain (present study); (b) simulation of HT in penetrating vessel network [9]; (c) healthy vessel; (d) BBB breakdown and haemorrhage modelling around a single vessel [7]. Figure adapted from Wang and Payne [7].

## 2. Materials and methods

The model consists of two components that simulate blood perfusion and individual haematomas respectively. The models will be introduced individually before being coupled. The methods to provide quantification of HT will then be introduced.

### *2.1. Perfusion model*

#### *2.1.1. Governing equations*

In the perfusion model, blood flow in the microcirculation is captured by a three-compartment porous medium (arteriole, capillary, and venule compartments) approach. Darcy's law is used to model the porous medium. The corresponding governing equations are:

$$\nabla \cdot \left( \frac{\boldsymbol{K_a}}{\mu_b} \nabla p_a \right) = \omega_{ac} \cdot (p_a - p_c), \tag{1}$$

$$\nabla \cdot \left( \frac{\boldsymbol{K_c}}{\mu_b} \nabla p_c \right) = -\omega_{ac} \cdot (p_a - p_c) + \omega_{cv} \cdot (p_c - p_v), \tag{2}$$

**Table 1**
Boundary conditions for the perfusion model.

| | Cortical Surface | Ventricle Surface |
|---|---|---|
| Arteriole Blood | $p_a = 90$mmHg (Non-occluded regions); $\mathbf{K_a}\nabla p_a = 0$ (Occluded regions, which are chosen manually to match the hematoma locations); | $\boldsymbol{K_a}\nabla p_a = 0$ |
| Capillary Blood | $\nabla p_c = 0$ | $\nabla p_c = 0$ |
| Venule Blood | $p_v = 15$ mmHg | $\boldsymbol{K_v}\nabla p_v = 0$ |

$$\nabla \cdot \left(\frac{\boldsymbol{K_v}}{\mu_b}\nabla p_v\right) = -\omega_{cv}\cdot(p_c - p_v), \tag{3}$$

where $p_a$, $p_c$ and $p_v$ denote the blood pressures in the arteriole, capillary, and venule compartments. $\boldsymbol{K_a}$, $\boldsymbol{K_c}$ and $\boldsymbol{K_v}$ denotes the permeability tensors for the arteriole, capillary, and venule compartments respectively, whereas $\omega_{ij}$ represents the fluid transfer coefficient between compartments $i$ and $j$, and $\mu_b$ denotes dynamic blood viscosity. Note that the transfer coefficients are different in white matter and grey matter and can thus be further defined by $\omega_{ac}^w$, $\omega_{cv}^w$ and $\omega_{ac}^g$, $\omega_{cv}^g$, respectively [17,20].

According to the results presented in previous studies [17,20], the permeability values in the arteriole and venule compartments are described using anisotropic permeability tensors since penetrating vessels are oriented perpendicular to the pial surface. In contrast, the permeability of the inter-connected capillary network is isotropic [17] and thus reduces to a scalar value.

*2.1.2. Boundary conditions*

In the cerebral blood circulation, blood feeds the brain through penetrating arterioles and flows back into the veins on the pial surface. Previous studies on cerebral blood perfusion show that each arterial vessel is responsible for the perfusion of a subregion on the pial surface [21,22]. Therefore, the brain pial surface is subdivided into 109 subregions and the subregions in the model can be used in this way to simulate vessel occlusions at different locations. The boundary conditions are then implemented as given in Table 1.

A constant pressure value is given to the non-occluded perfusion regions while no-flow boundary conditions are given on the occluded subregions. The occluded subregions are chosen to match locations of the hematoma based on the clinical images. Since blood cannot flow through the ventricular surface, zero flux Neumann boundary conditions are imposed on the ventricle surface for all three compartments.

*2.2. Leakage model*

*2.2.1. Governing equations*

In this model, the blood is assumed to leak into the interstitial space and an additional compartment for the interstitial flow is thus required. Therefore, a porous circulation model with 4 compartments (arteriole, capillary network, venule, and interstitial space) is proposed here to predict the growth of a hematoma and the change in cerebral blood flow (CBF) and perfusion before and after HT. The blood leakage is modelled using the capillary wall filtration model and the flow rate can be written as [23,24]:

$$S = \begin{cases} 2\bar{n}_b\frac{L_p}{R_c}(p_c - p_w) \ \textit{in bleeding tissue} \\ 0 \ \textit{in healthy tissue} \end{cases} \tag{4}$$

where $\bar{n}_b$ is the volume fraction of blood vessel in a unit volume of brain tissue, $L_p$ denotes the vascular permeability, $R_c$ denotes vessel radius, $p$ denotes the hydrostatic pressure with subscripts that represent capillary blood pressure and interstitial fluid pressure respectively and $S$ denotes the leakage flow rate.

Here, the compression of the capillary blood vessels is also considered using the tube law [24,25], and the capillary compression function is assumed to be of the form:

$$f = \frac{1}{2}\left[1 + \tanh\left(1 + \frac{\bar{p} - p_w}{0.01E}\right)\right] \tag{5}$$

where $f$ denotes the fraction of vessels remaining open, $\bar{p}$ is the baseline value of interstitial pressure, and $E = 6.5$mmHg is the bulk modulus representing the capillary wall stiffness.

Since the blood flow into the haematoma compresses the tissue, it acts to squeeze the interstitial fluid in the brain. Therefore, the blood flow and the interstitial flow driven by the growing haematoma both need to be considered. There are no current experimental data available to define the surface of a haematoma. Hence, in these simulations, in order to obtain reasonable values of haematoma volume, we set the threshold of haematoma surface pressure, $p^* = 3.5$mmHg

**Table 2**
Boundary conditions for the haematoma model.

| | Cortical Surface | Ventricle Surface |
|---|---|---|
| Arteriole Blood | $p_a = 90$ mmHg | $\boldsymbol{K_a}\nabla p_a = 0$ |
| Capillary Blood | $\nabla p_c = 0$ | $\nabla p_c = 0$ |
| Venule Blood | $p_v = 15$ mmHg | $\boldsymbol{K_v}\nabla p_v = 0$ |
| Interstitial Fluid | $p_w = 10$ mmHg | $p_w = 10$ mmHg |

above the baseline tissue pressure. The value is chosen following simulations (results shown below) that show that this value appears to be the optimal one to obtain haematoma volumes that match clinical imaging data reasonably well. The sensitivity analysis for this haematoma surface pressure will, however, be presented and discussed below.

Based on our knowledge, there is currently no anatomical data of the bleeding proportion in different types of vessels in HT. In this model, we assumed that only the capillaries are leaky when HT occurs. Gliem et al. [26] found that bleeding frequently occurred around thin-walled vessel in the infarct border zone and the capillary wall thickness is around 2 um [27]. In addition, based on morphological measurements of the frequency distribution of vessels diameter, majority of vessels are found to be capillary vessels [28]. Furthermore, Wang et al. [9] found that the larger leaky vessels led to larger haematoma volume and in this simulation, the PH2 type of HT is excluded. Therefore, to determine the bleeding regions in different compartments (arteries, capillaries and veins), we assume that the leakage only occurs in the capillary compartment.

The governing equations for the leakage model can be written as the following:

$$\nabla \cdot \left(\frac{K}{\mu}\nabla p_w\right) = -f \cdot S \tag{6}$$

$$\nabla \cdot \left(\frac{\boldsymbol{K_a}}{\mu_b}\nabla p_a\right) = \quad f \cdot \omega_{ac} \cdot (p_a - p_c) \tag{7}$$

$$\nabla \cdot \left(\frac{K_c}{\mu_b}\nabla p_c\right) = \; - \; f \cdot \omega_{ac} \cdot (p_a - p_c) + f \cdot \omega_{cv} \cdot (p_c - p_v) \; + \; f \cdot S \tag{8}$$

$$\nabla \cdot \left(\frac{\boldsymbol{K_v}}{\mu_b}\nabla p_v\right) = \; - \; f \cdot \omega_{cv} \cdot (p_c - p_v) \tag{9}$$

where $\mu$ denotes fluid viscosity in the interstitial space.

The permeability of fluid in the interstitial space depends on whether the space is occupied by blood or interstitial fluid. Since the fluid component is assumed to be determined by a pressure threshold $p^* = 3.5$ mmHg, the tissue permeability of fluid in the interstitial space depends on pressure values and it is thus assumed to be of the form:

$$\frac{K}{\mu} = \frac{K_w}{\mu} + \frac{1}{2}\left(\frac{K_b}{\mu} - \frac{K_w}{\mu}\right) \cdot \left[1 + \tanh\left(1 + \frac{\bar{p} - p_w}{p^*}\right)\right] \tag{10}$$

where $K_w$ and $K_b$ denote the conductivities of water and blood in the interstitial space, respectively.

*2.2.2. Boundary conditions*

In the haematoma model, following recanalization, the blood perfusion is assumed to be fully restored. Although this is a strong assumption imposed for simplicity, it will be possible in future to examine the effect of incomplete restoration. The perfusion then leads to an increased blood pressure on the blood vessel wall and causes vessel rupture and the formation of a haematoma. Constant pressure boundary conditions are imposed on the pial surface for all subregions. The interstitial space boundaries are the interface between interstitial fluid and cerebrospinal fluid and the pressure is assumed to be constant due to the high compliance of the cerebrospinal fluid (CSF) [29]. The boundary conditions for the haematoma model are given in Table 2.

*2.3. Model coupling*

In the perfusion model, it is assumed that the locations with higher values of capillary blood pressure are prone to vessel disruption, BBB breakdown, and consequently HT. Since haematoma is likely only to occur in the infarcted region, a 70% perfusion reduction is used as the primary threshold for the tissue bleeding [30–32]. Furthermore, although subcortical HT has been found to appear more frequently than cortical HT, it should be noted that the prediction of the precise spatial location of the haematoma is highly challenging. To obtain the haematoma locations that match the clinical images, capillary pressure ranges were varied and used as the secondary threshold for vessel rupture and tissue bleeding. The geometry of the bleeding tissue obtained from the perfusion model was then included within the leakage model to simulate the growth of the haematoma and the resulting perfusion reduction.

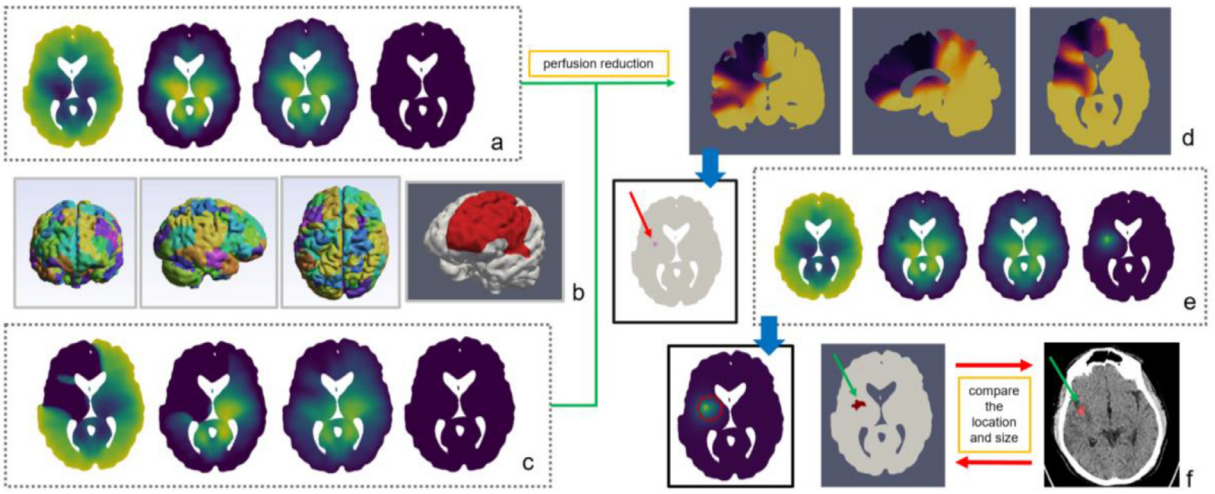


**Fig. 2.** (a) Simulation of blood pressures in healthy blood flow in the arteriole, capillary, venule and interstitial space, respectively. (b) Subregions on the cortical surface and selection of the occluded regions (red). (c) Simulation of brain blood pressures in infarction. A reduction in blood pressures in the occluded region is shown as the colour darkens. (d) Blood perfusion reduction obtained from the healthy and stroke cases. (e) Bleeding tissue is assumed to occur in the regions where perfusion reduction is over 70% and is chosen by varying the capillary blood pressure ranges. The bleeding tissue is then imported into the leakage model for the simulation of the growth of hematoma. (f) 3.5 mmHg of pressure rise is used as the threshold of hematoma boundary and the hematoma is compared with the CT images.

**Table 3**
Values of model parameters used in the perfusion, oedema and osmotherapy models and their sources.

| Parameter | Value | Refs. |
|---|---|---|
| $\mathbf{K_a}$ | $4.4424 \times 10^{-12}$ m$^2$ | Estimated by 0-order arteriole diameters and vessel density [17] |
| $K_c$ | $1.5408 \times 10^{-14}$ m$^2$ | $1.0 \times 10^{-15}$ m$^2$[20]; $1.0 \times 10^{-10}$ m$^2$ [33] |
| $\mathbf{K_v}$ | $8.8848 \times 10^{-12}$ m$^2$ | Estimated by pressure and blood perfusion rate [17] |
| $K_w$ | $3.6 \times 10^{-15}$ m$^2$ | [34] |
| $K_b$ | $1.0 \times 10^{-15}$ m$^2$ | [34] |
| $\omega_{ac}^{w}$ | $1.326 \times 10^{-6}$ Pa$^{-1} \cdot$ s$^{-1}$ | Derived from perfusion rates in grey and white matter [17,35] |
| $\omega_{ac}^{g}$ | $5.22 \times 10^{-7}$ Pa$^{-1} \cdot$ s$^{-1}$ | |
| $\omega_{cv}^{w}$ | $4.641 \times 10^{-7}$ Pa$^{-1} \cdot$ s$^{-1}$ | |
| $\omega_{cv}^{g}$ | $1.828 \times 10^{-6}$ Pa$^{-1} \cdot$ s$^{-1}$ | |
| $p_a$ at cortical surface | 12, 000 $Pa$ = 90 mmHg | [17] |
| $\bar{p}$ | 10 mmHg | [36] |
| $p_v$ at cortical surface | 2000 $Pa$ = 15 mmHg | [17] |
| $L_p$ | $3.0 \times 10^{-11}$ m $\cdot$ Pa$^{-1} \cdot$ s$^{-1}$ | [34] |
| $R_c$ | $5.0 \times 10^{-6}$m | [37] |
| $\bar{n}_b$ | 0.03 | [38] |
| $\mu_b$ | $3.6 \times 10^{-3}$Pa $\cdot$ s | [34] |
| $\mu$ | $1.0 \times 10^{-3}$Pa $\cdot$ s | [15] |

1. The heathy perfusion is simulated to obtain the healthy blood flow (Fig. 2a).
2. The occluded subregions are chosen (Fig. 2b) to obtain the stroke blood perfusion (Fig. 2c).
3. Patient-specific capillary pressure ranges are chosen manually. Regions with 70% perfusion reduction (Fig. 2d) and over where the capillary blood pressure lie in the ranges are defined as bleeding tissue for each patient.
4. The regions chosen as bleeding tissue are imported into the leakage model for haematoma simulation (Fig. 2e).
5. The haematomas are defined as regions with interstitial pressure rise over 3.5 mmHg. Comparison in the pairs of haematoma centre locations $(x_i, y_i, z_i)$ and volumes, which are obtained from the computational model and clinical images is performed (Fig. 2f). If the differences do not lie in a reasonable range (the differences in pairs of $x$ values, $y$ values and $z$ values from the computational model and imaging data are $< 5\%$), then go back to step 2 until a reasonable hematoma is obtained.

All the parameters used in the models and their sources are given in full in Table 3.

In the model, the governing equations are solved numerically using Python with a high-performance open-source Finite Element library, FEniCS [39,40].The highly coupled equations in the Finite Element model are solved in a mixed function space describing the multi-compartment dynamic system. The pressure in each compartment ($p_i$) is discretised with piecewise linear Lagrange (P1) elements. Meanwhile, the permeabilities ($\boldsymbol{K}_i$) and the other coefficients ($\omega_{ij}$, $L_p$, etc.) used in the model are represented in piecewise constant (dP0) tensor and scalar function spaces, respectively. The flow fields and the

blood perfusion are computed in dP0 elements and are solved using the BiCojungate Gradient STABilised method (BiCGSTAB) with an Algebraic MultiGrid (AMG) preconditioner.

### 2.4. Quantifications of CT images

We included patients with HT from the MR CLEAN–NO IV trial [18]. The MR CLEAN–NO IV trial was a multicentre randomized controlled trial that assessed the effect of endovascular therapy (EVT; intervention arm) alone compared with intravenous alteplase (IVT) followed by EVT (control arm) for acute ischaemic stroke due to anterior circulation large vessel occlusion, in patients presenting to EVT-capable centres within 4.5 h of stroke onset. The full study protocol of MR CLEAN–NO IV has previously been described by Treurniet et al. [41]. HT was assessed on follow-up CT acquired within 7 days after stroke onset, according to the Heidelberg bleeding classification [18,41]. We included 5 patients with HI1, 5 with HI2 and 5 with PH1, as adjusted by MR CLEAN–NO IV core lab. We did not include patients with PH2 because in these patients there were significant tissue displacements and large MLS, which are more difficult to simulate (and may require a non-linear constitutive model for the tissue). All haemorrhages in the 15 series of CT images were quantified by manually delineating the haemorrhage by a trained observer (KRK) using ITK-SNAP (version 3.4.0).

All CT images were imported into MATLAB R2022a to rebuild a pixel (2D) matrix, which was used to determine the centre of each haematoma. A coordinate was established to describe hematoma centres, as shown in Figs. 3 and 4. The origin is set at the lower left of the cerebellum (inferior left end of the medulla oblongata) for all patients and computational brain models. We found that it was challenging to determine the centre of the brain when there is a significant effect of MLS shown in the imaging data. Thus, setting the origin outside the brain based on the boundary of the brain became our preferred choice. The centre of the haematoma in the brain can thus be described in a three-dimensional co-ordinate of the form $(x,\ y,\ z)$ where $x$, $y$ and $z$ lie in the range of $0 - 100\%$.

The determination of the haematoma location is based on the delineation of the haemorrhage. The haematoma could then be quantified in the pixel matrix. The pixels of the haematoma shown in the pixel matrix can be described as $(x_i, y_i, z_i)$. Then all the locations of haematoma pixels in three directions were used to obtain the centre of each haematoma. The flow diagram of the quantification of HT method is shown in Fig. 3.

## 3. Results

### 3.1. Haematoma location and volume measurements

Using Eqs. (4)–(10), the haematoma models can be computed for each patient with different sizes and locations of HT. An example of a HT simulation is given in Fig. 4 for a type HI2 haematoma. The total haematoma volume from CT images was calculated to be 0.72 ml and the result obtained from the simulation shows that the haematoma volume is close at 0.64 ml. The centre of haematoma obtained from the CT images is located at (25.82%, 60.60%, 48.72%) and that calculated from the simulation is located at (29.48%, 61.65%, 47.17%). As discussed above, the co-ordinates of each haematoma centre are given in percentage length (i.e., a dimensionless length) to mitigate the effects of brain geometry that may vary from one patient to another. Fig. 5 shows the correlation of haematoma and bleeding region (note that the example shown in this figure is not the same as the example in Fig. 4). It can be seen that the bleeding region (white) is located completely inside the haematoma (red).

These 15 HT imaging data were chosen because of their high image quality. As shown in Fig. 6(a), 5 patients had HT in the left hemisphere ($x$ value $< 50\%$) and 10 patients had HT in the right hemisphere. The haematoma centres obtained from the image data and simulations are all close to each other (no significantly statistical differences are found using a $t$-test).

The co-ordinate differences from simulations and CT images occur because our model is limited in its location of the haematoma since the subregion size was pre-determined, i.e., the finite resolutions of both the CT images and the computational brain model lead to small differences in the haematoma centres [17]. Comparisons of haematoma volumes ($V$) are also shown in Fig. 6(b) and the p-value for the pair of volumes is $> 0.05$, indicating that there is again no statistically significant difference between the predicted and measured haematoma volumes.

### 3.2. Perfusion deficit quantification

Fig. 7 shows the comparison of perfusion reduction. In these simulations, we find that perfusion reduces by $5 - 16\%$ after HT onset. The perfusion reduction ($\Delta F$) (from the full brain model) is computed from data collected on the ipsilateral side compared with the contralateral (healthy) side. The right part of Fig. 7 shows the perfusion reduction values computed in a penetrating network model, the values of which are taken from Wang et al. [9].

### 3.3. Sensitivity analysis

We next used one example of HT to process the sensitivity analysis with various values of blood viscosity $\mu_b$, the definition of haematoma surface pressure $p^*$ and blood pressure $p_a$. This example of HT was set close to the lenticular nucleus, which is found to be a high occurrence location of HT [42]. Correlations between haematoma volumes ($V$) and perfusion

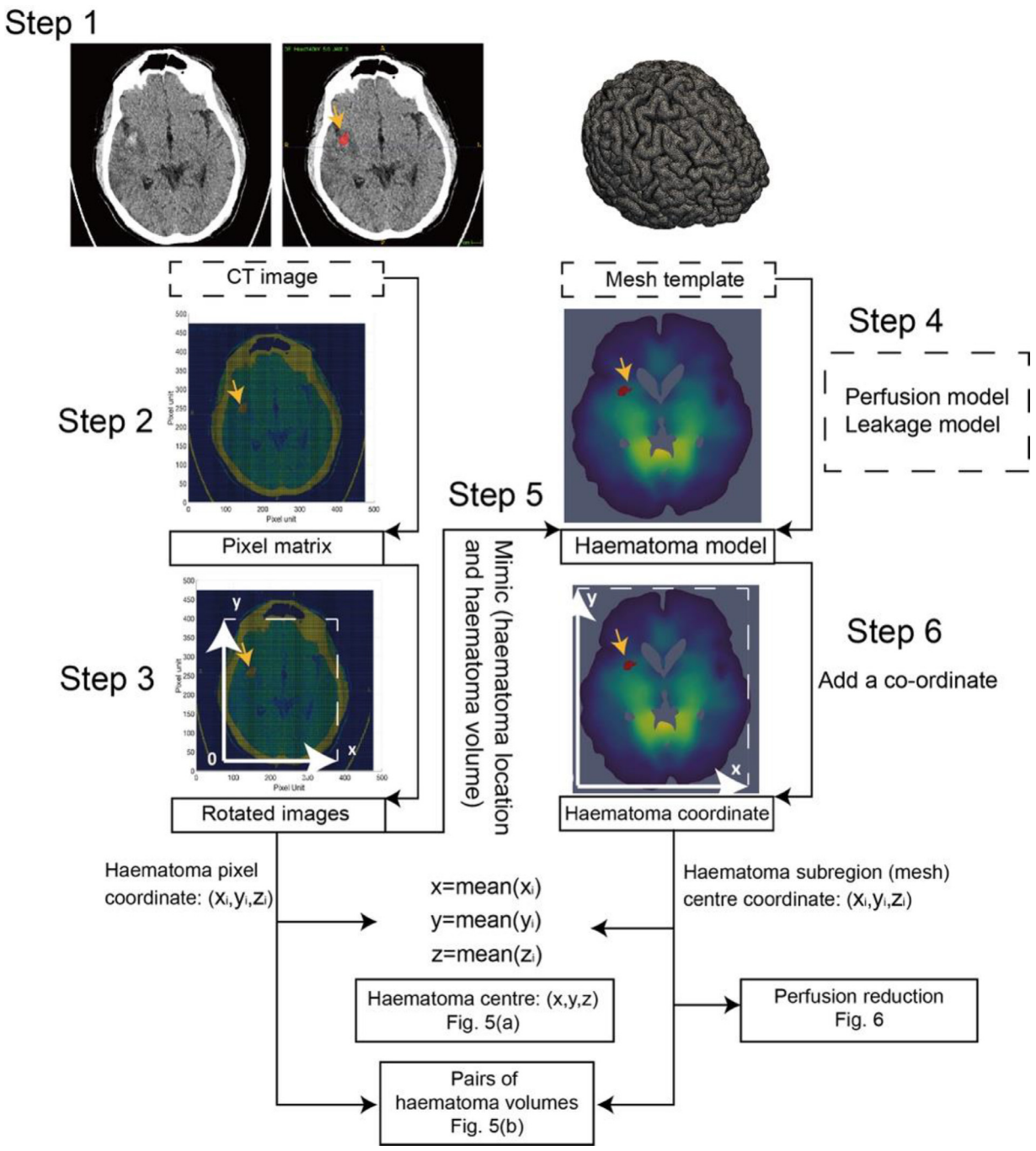


**Fig. 3.** Schematic drawing of quantification method of HT for both CT images and the computational brain model. Dashed boxes: input. Yellow arrows: haematoma locations. The image was rotated after being imported into MATLAB using the function "imrotate" in MATLAB to ensure the same size (dimensions) of matrix.

reduction ($\Delta F$) with $\mu_b$, $p^*$, $p_a$ and $L_p$ were tested, as shown in Fig. 8. A critical phenomenon that was found when we adjusted the blood viscosity was that the haematoma volume increases with increased blood viscosity when the blood viscosity is in the range of $3.4 - 4.1$ cP. It is found that 1% increase in blood viscosity increases haematoma volume by 10.35% from the baseline (when $\mu_b = 3.6$ cP), as shown in Fig. 8(b). In addition, we find that the perfusion reduces when the blood viscosity increases: 1% increase of blood viscosity causes a reduction of 0.04% in perfusion, Fig. 8(b).

As shown in Fig. 8(c), a higher definition of haematoma surface pressure leads to a larger haematoma volume and smaller perfusion reduction, as would be expected (note the logarithmic scale, which indicates the very high sensitivity).

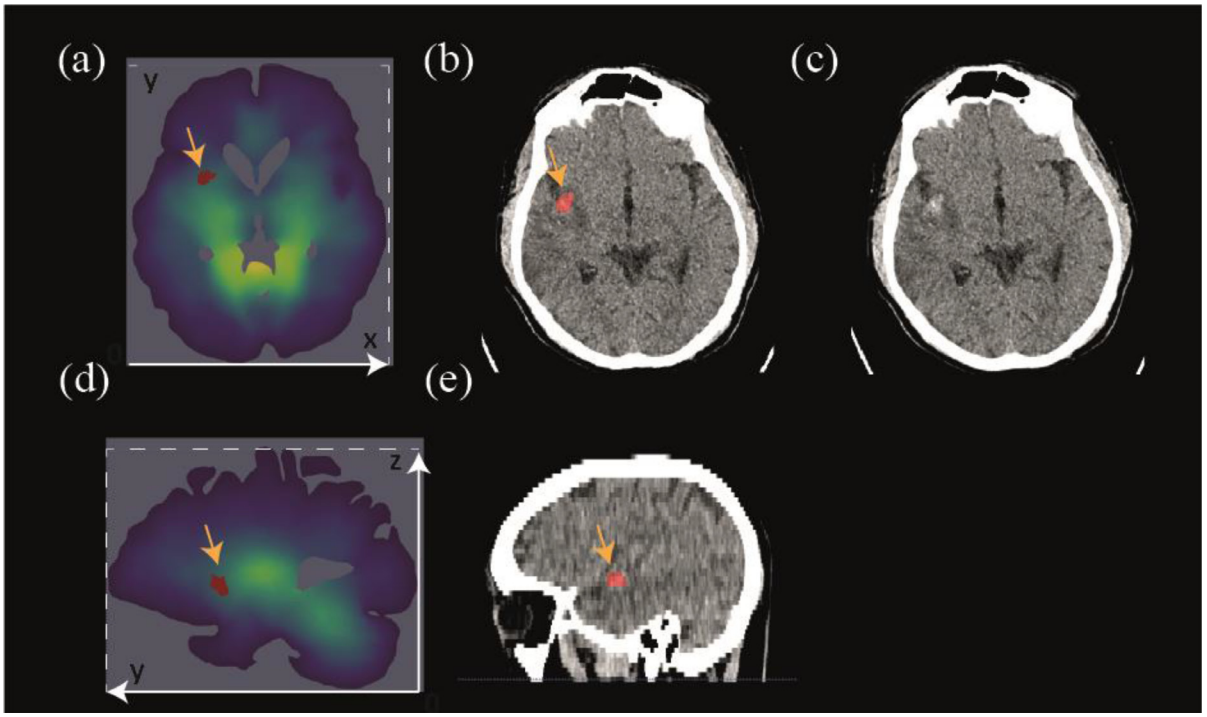


**Fig. 4.** Example HT model showing a haematoma located in a full brain model obtained from the axial plane (a) and sagittal plane (d). This example is compared with an example of HT by showing the axial plane (b) and sagittal plane (e). The positive x-axis extends to the right, reaching the far-right side of the brain; the positive y-axis extends to the front, reaching the front side of the brain; and the positive z-axis extends to the top of the brain. The CT image without annotation (c).

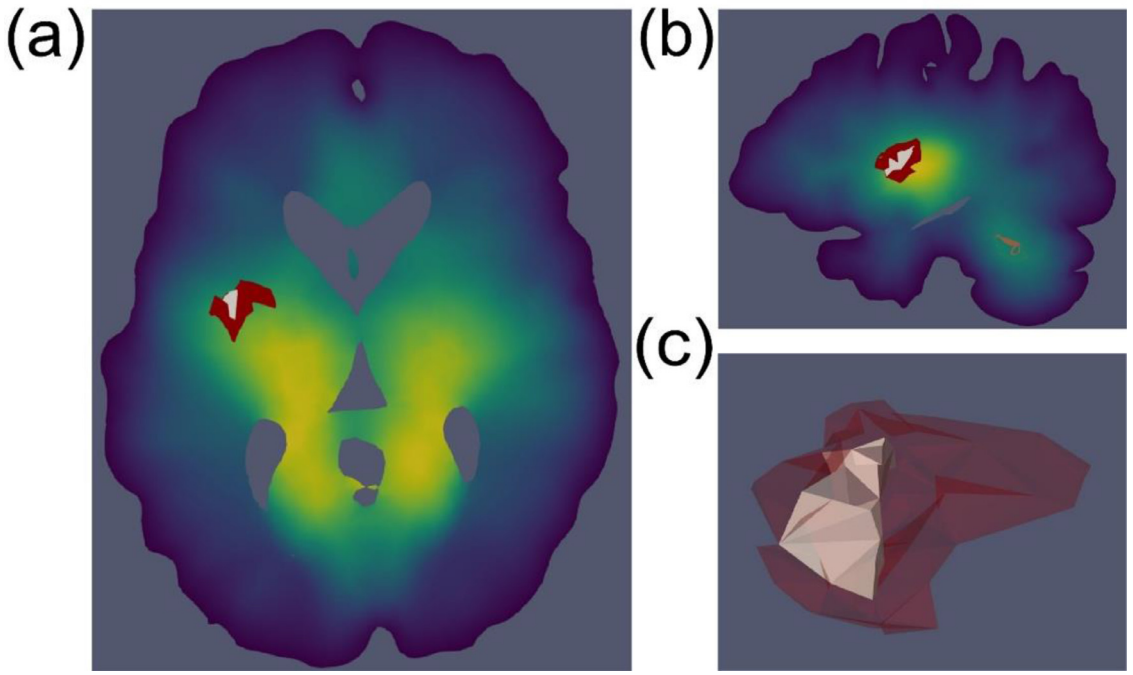


**Fig. 5.** Example of haematoma and bleeding region. A haematoma (red substance) including bleeding region (white substance) from the axial plane (a). Slice view of the haematoma and bleeding region obtained from the simulation (b). The haematoma and bleeding region are shown overlaid in (c). The bleeding region is fully inside the haematoma.

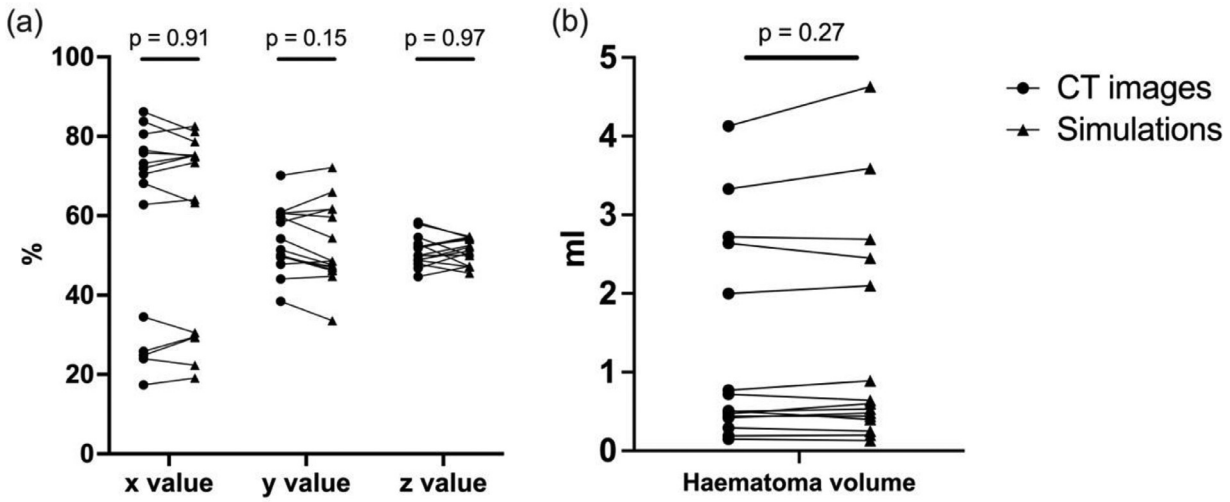


**Fig. 6.** Comparison of HT between CT images and simulations. Quantification of haematoma centres in *x*, *y* and *z* axis (a). Comparison of haematoma volume between image data and simulations (b).

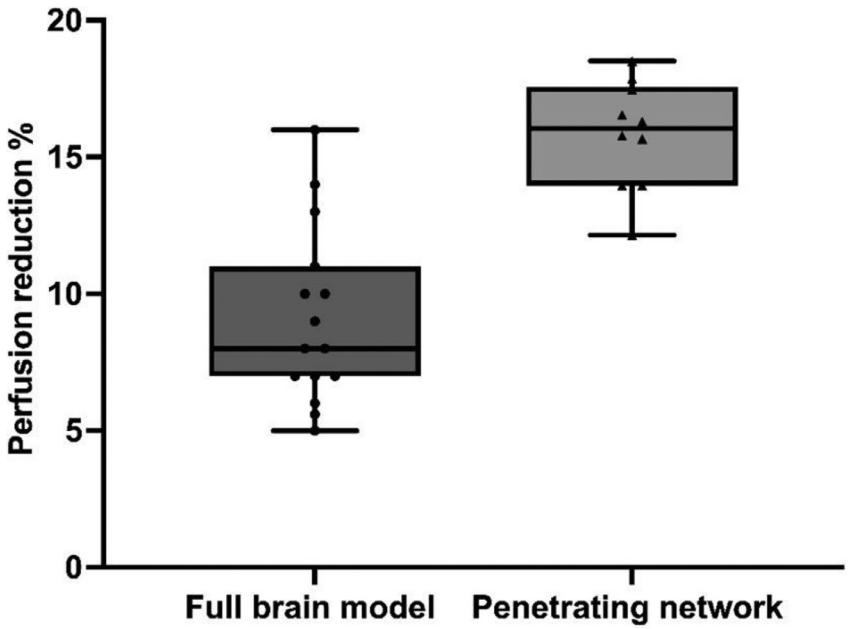


**Fig. 7.** Comparison of perfusion reduction obtained from this full brain model and penetrating network model. The data for right boxplot are reproduced from Wang et al. [9].

The haematoma volume changes significantly with the definition of haematoma surface pressure $p^*$. Haematoma volume is calculated to be 10.02ml when we set $p^*$ as the initial value at 1mmHg. When the value of $p^*$is set at 5mmHg, the haematoma volume is equal to 0.05ml. When the value of $p^*$ is thus set to be just 5 times larger than its original value, the haematoma volume will decrease by some four orders of magnitude. As shown in Fig. 8(d), 1% change of $p^*$ ($\pm p'$) leads to 0.0061% change in perfusion.

Higher blood pressure, as expected, results in larger perfusion reduction and haematoma volume. As shown in Fig. 8(e), when the blood pressure $p_a$ is set from 70mmHg to 90*mmHg*, the haematoma volume grows from 0.51ml to 1.12ml and perfusion reduction increases from 0.28% to 22.85%. The measure of importance is shown in Fig. 8(f): 1% increase of blood pressure reduces 0.80% of perfusion and increases 4.73% of haematoma volume from the baseline.

Higher hydraulic permeability results in larger perfusion reduction and haematoma volume, as shown in Fig. 8(g) and 8(h). When the permeability increased by four orders of magnitude from $10^{-12}$ m/(Pa · S), the perfusion reduction increased from 7.89% to 16.7% and the haematoma volume increased from 0.017ml to 0.66ml.

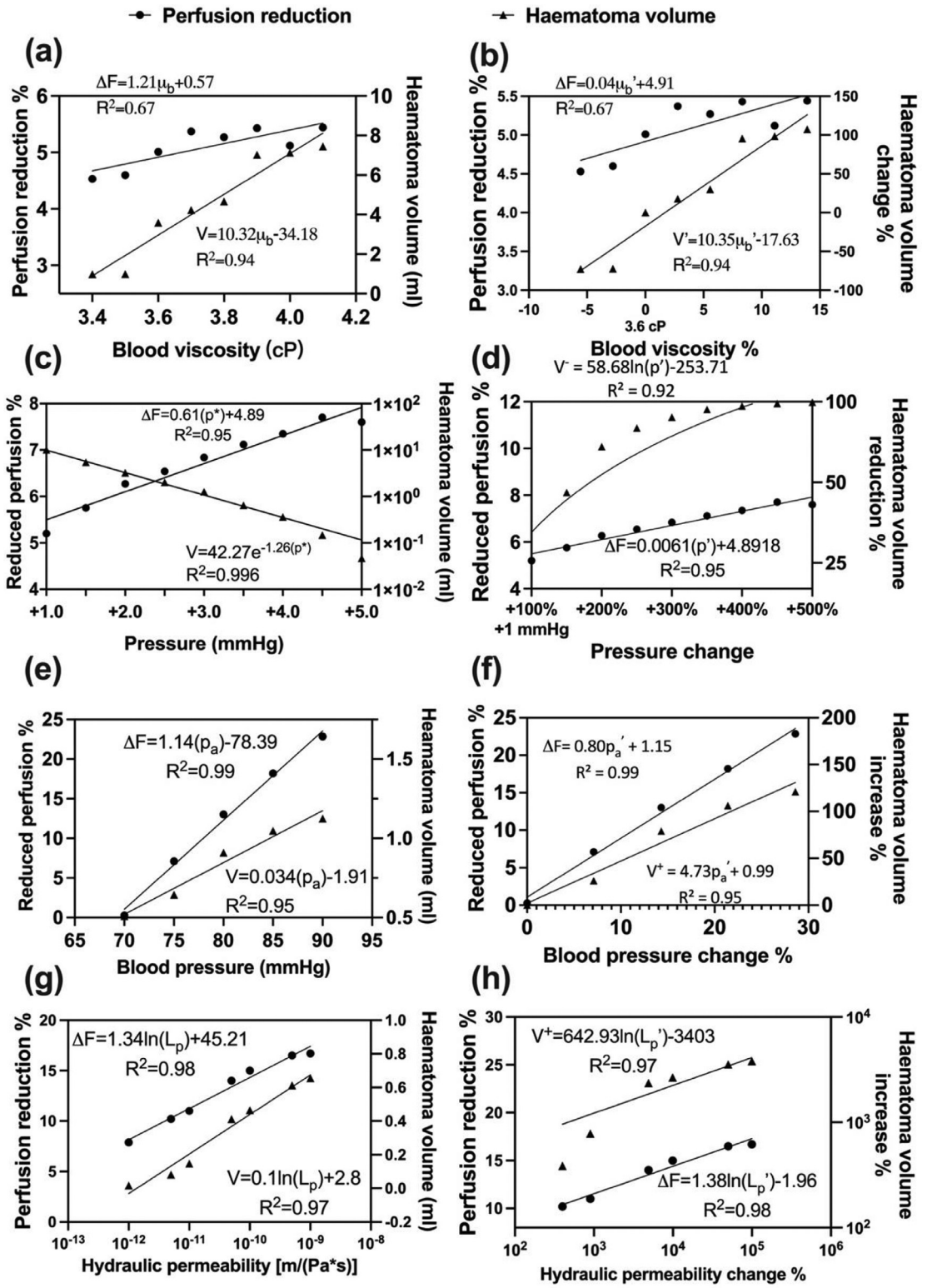


**Fig. 8.** Variations in perfusion reduction and haematoma volume as functions of (a) blood viscosity, (c) the definition of haematoma surface pressure, (e) blood pressure (source pressure) and (g) hydraulic permeability. Measures of importance of perfusion reduction and haematoma volume change as functions of (b) viscosity change, (d) the definition of haematoma surface pressure change, (f) blood pressure change, (h) hydraulic permeability. $\Delta F$ denotes perfusion reduction. $V$ denotes the haematoma volume, $V'$ denotes the haematoma volume change. $V^-$ denotes reduced haematoma volume and $V^+$ denotes increased haematoma volume. $\mu_b'$ denotes the blood viscosity change, $p'$ denotes the definition of haematoma surface pressure change and $p_a'$ denotes the blood pressure change. Note that the right y axis in (c) is shown in logarithmic scale at a base of $e$.

## 4. Discussion

In this study, we have developed a model of HT in a full brain model to examine the relationship between the bleeding region with HT and to investigate how HT can be affected by various haemodynamic parameters. This simulation is based on the model proposed by Wang and Payne [7], which presents a mathematical model of HT after ischaemic stroke. They investigated how changes in vascular geometry can affect the severity of HT. To further develop these simulations, Wang et al. [9] simulated the HT in a penetrating network to determine how HT can affect healthy blood vessels and tissues. In this study, we have further developed this HT model into a computational whole brain model to investigate the correlation between bleeding region and haematoma. We quantified the HT and validated the results with a set of clinical images to simulate the bleeding region of the haematomas. By using the optimised parameters, we established a HT scenario to investigate the haemodynamic factors that may affect HT.

In the quantification of HT for real clinical image data, we controlled the haematoma volumes and centres by adjusting the infarcted regions and capillary pressure manually to approach the haematoma volumes and centres obtained from CT images. The coordinate points of haematoma centres both from these models and CT images are compared in Fig. 6(a) by $t$-test. All p-values of $x$, $y$ and $z$ values of haematoma centres are $> 0.05$. Aligning the y-values, however, proved to be relatively difficult compared to processing the other two values. This is due to different patients having different geometries of brains; thus, the origin of the coordinate system will be slightly different comparing with the computational model, i.e., the accurate coordinate of the inferior left end of the medulla oblongata is challenging to determine. In addition, the resolution of the computational brain subregion also leads to some differences. This should be addressed more rigorously in the future.

The voxel-based dice similarity coefficient (DSC), which was proposed by Dice [43], is commonly used to quantify the area overlap between the algorithm and manually segmented regions for patients with various diseases [44–48]. However, DSC can only be calculated based on two images shown by pixels or voxels. In our study, the computational brain model is mesh-based, whereas the CT images are pixel-based. Thus, the overlap regions of HT from the computational brain model and CT images are difficult to determine and define. In addition, it is challenging to determine the region of interest since the anatomical geometries of patients' brains vary from one patient to another.

In this study, the location and the volume of haematoma are the primary focus. However, the shape of the haematoma is not validated with the CT images since the main aim of this study is to optimise the model parameters (for example, $p^*$) and to investigate the factors that may influence the severity of HT. We suggest, however, that the shape of the haematoma should be determined in the next study to locate the bleeding region more accurately. DSC [43] (to determine the overlap) and symmetric correspondence method [49] (to obtain the difference in boundaries) are potential ways to quantify the shape difference.

In the comparison of the haematoma volumes between the CT scan and the computational model, no statistically significant difference was found. The results of haematoma volumes from the simulations are close to the clinical data. From the 15 patients, 5 had HI1, 5 had HI2 and 5 had PH1. All haematoma volumes are less than 5ml. We did not split up results into the different types since we used these imaging data to optimise our model parameters. Different types of HT provide nearly the same results, for example, the optimised $p^*$ was found to be 3.5mmHg for all types of HT. We did not include the PH2 patients at this stage since this model is not able to investigate HT with large tissue displacement, especially for patients with a significant MLS.

As shown in Fig. 7, a reduction in perfusion is found following HT, in the range of $5 - 16\%$. Jain et al. [19] compared the CT perfusion parameters for a control group and an HT group: the mean reduction rate of relative cerebral blood flow (rCBF) was found to be $\pm$ 4.3% (5.7 – 14.3%), which is in good agreement with the results that we present here (note this experimental result of rCBF is not obtained from MR CLEAN–NO IV). Since rCBF was calculated clinically from data collected on the ipsilateral side compared with the contralateral (healthy) side, we used the same method to determine the reduction of perfusion in these simulations (noting that the comparison is not exact).

Wang et al. [9] predicted that the reduction of perfusion in a penetrating network voxel, which is in the size of $1 \times 1 \times 2.5$mm, is approximately $13 - 17\%$ after HT onset. Our results are found to be smaller than the perfusion reduction from the penetrating network. We suggest that this is because different sizes of regions of interest are selected.

In this study, our results show that increased blood viscosity has the potential to increase the volumes of haematoma. Çinar et al. [50] measured the correlations between blood glucose with blood viscosity: when the mean value of blood glucose increased from $100 - 400$mg/dL, viscosity increased by 25% ($r = 0.59$, $P = 0.002$). Mushtaq et al. [51] also found that hyperglycaemia is associated with blood viscosity. A phenomenon that increased baseline glucose levels were associated with overall symptomatic intracerebral haemorrhage (sICH) occurrence was proposed by van der Steen et al. [52] . The simulations from our model support the hypothesis that increased blood glucose levels lead to a higher level of severity of HT if the high blood glucose level results in higher blood viscosity.

In addition, high blood glucose and high blood pressure are linked, since high levels of sugar in blood can lead to atherosclerosis [53–55]. As shown in Fig. 8(e), higher blood pressure leads to a larger haematoma and a larger reduction in perfusion, as would be expected. Blood pressure acts as a driving force of HT in our model. Our results thus also support the results proposed by van der Steen et al. [52]: i.e., that increased baseline systolic blood pressures can increase overall sICH occurrence.

It should be noted that in our simulation, the time dynamics were not included since all images were taken at the time of CT scanning. Thus, the dynamic process of haemostasis was not considered. However, one important aspect of a reduction in cerebral blood volume (CBV) caused by haemostasis should be considered in the following stages of model development due to localized vasoconstriction occurring before haemostasis starts [56]. Localized vasoconstriction caused by haemostasis could also lead to significant capillary compression but here it was assumed that increased intracranial pressure (ICP) was the primary source of reduced CBV. It also indicates that further studies are needed to determine the dynamic correlations between variations in perfusion reduction and haematoma volume.

To the best of our knowledge, there are very limited available experimental data that propose rigorous definitions of the haematoma boundary using physical parameters after HT onset, especially for HT in the full brain. Wang and Payne [7] and Wang et al. [9] set the definition of haematoma boundary at 0.1mmHg above tissue pressure, which was found to ensure a haematoma radius close to experimental data in mice: Jenkins et al. [57] measured the distance between the haematoma boundary and related damaged vessels as 700$\mu$m. However, these simulations were based on a single leaky vessel and in relatively small regions of interest, compared to our full brain model.

It can be seen from Fig. 8(c) that haematoma volume is highly sensitive to the definition of haematoma boundary pressure. Since the haematoma boundary was drawn manually from clinical imaging data, the identification of the haematoma boundary may be different from the haematoma definition based on experimental data from individual vessels in mice [7,57]. To keep the size of haematoma volume to a reasonable size compared with clinical data [18,41], we optimised the definition of haematoma surface pressure, $p^*$, and found this to be 3.5mmHg above tissue pressure in our simulation.

Regarding the identifiability aspects of the model, nearly all the parameters that we are using here are likely to vary from one patient to another (to a greater or lesser degree). We suspect that the hydraulic permeability $L_p$ is one of the most likely values to vary significantly from one patient to another, although obtaining experimental measurements of this parameter is highly challenging. The sensitivity analysis for the hydraulic permeability $L_p$ is shown in Fig. 8(g) and (h). Future work will be required to confirm the hydraulic permeability for different types and locations of HT, which will be required to predicting the severity of HT more accurately.

In addition, we have only one computational brain model with a specific shape, while the geometries of patient brains vary from one patient to another. Although the coordinate points of haematoma centres (described using percentage values) were used in our simulation to eliminate the influence of the different shapes between our brain model and real patients' brains, more adaptive brain models will be needed in the future to fit different brain shapes. One of the potential models has been proposed by Jozsa et al. [58]: the anatomical (geometrical) fitness of the brain models was evaluated by comparing the simulated grey and white matter volumes to measurements in healthy reference subjects. Thus, various patients can be compared with every computational brain which is adjusted to geometry. We can use the same method in future to fit our brain model with specific patient brains.

As shown in Fig. 5, the bleeding region and haematoma are both present in the brain model. However, this model is not able to locate the specific bleeding vessels. Since the vessel geometry varies from one patient to another, it is challenging to determine the bleeding vessels. It is suggested that the bleeding regions will need to be validated in the future as and when the relevant clinical data become available.

The long-term aim of our work is to identify those patients who are most at risk of haemorrhage based on imaging data (and other non-imaging parameters) and to predict the occurrence and severity of HT. However, our model still has many limitations to predict HT. One of the potential methods to develop a prediction model is linking HT with oedema. Oedema and HT were found to be highly associated after stroke and oedema was commonly assumed as a leading factor of HT [59]. In addition, oedema could potentially be examined and identified by a wearable ultrasound device such as that invented by Wang et al. [60]. Thus, HT could in future become much more predictable by applying a wearable ultrasound device combined with our model relating oedema and haematoma.

## 5. Conclusion

Through the development of a mathematical model to simulate HT in a computational brain model, validation with real clinical images is possible through the comparison between haematoma geometry, locations, and perfusion change. This study has identified that a reduction in perfusion after HT onset is in the range of $5 - 16\%$, which is with good agreement with experimental data. One of the more significant results found here is that increased blood glucose level and high blood pressure potentially lead to more severe HT, as observed clinically, according to:

- 1% increase in blood viscosity reduces perfusion by 0.04% and increases haematoma volume by 10.35% from baseline.
- 1% increase in blood pressure reduces perfusion by 0.80% and increases haematoma volume by 4.73% from baseline.

This model is the first such to be able to simulate the correlation between bleeding regions and haematoma and should be of assistance in future assessment of HT for clinicians.

## Data availability

Data will be made available on request.

## References


[1] M. Katan, A. Luft, in: Global burden of stroke, 2018, pp. 208–211. Thieme Medical Publishers.
[2] J. Álvarez-Sabín, O. Maisterra, E. Santamarina, C.S. Kase, Factors influencing haemorrhagic transformation in ischaemic stroke, Lancet Neurol. 12 (2013) 689–705.
[3] E.B. Marsh, R.H. Llinas, A.E. Hillis, R.F. Gottesman, Hemorrhagic transformation in patients with acute ischaemic stroke and an indication for anticoagulation, Eur. J. Neurol. 20 (2013) 962–967.
[4] R. von Kummer, J.P. Broderick, B.C. Campbell, A. Demchuk, M. Goyal, M.D. Hill, K.M. Treurniet, C.B. Majoie, H.A. Marquering, M.V. Mazya, The Heidelberg bleeding classification: classification of bleeding events after ischemic stroke and reperfusion therapy, Stroke 46 (2015) 2981–2986.
[5] K.R. van Kranendonk, K.M. Treurniet, A.M. Boers, O.A. Berkhemer, J.M. Coutinho, H.F. Lingsma, W.H. Van Zwam, A. van der Lugt, R.J. van Oostenbrugge, D.W. Dippel, Added prognostic value of hemorrhagic transformation quantification in patients with acute ischemic stroke, Front. Neurol. 11 (2020) 1335.
[6] H.W. Nah, S.U. Kwon, D.W. Kang, J.S. Ahn, B.D. Kwun, J.S. Kim, Moyamoya disease-related versus primary intracerebral hemorrhage: location and outcomes are different, Stroke 43 (2012) 1947–1950.
[7] J. Wang, S.J. Payne, Mathematical modelling of haemorrhagic transformation after ischaemic stroke, J. Theor. Biol. (2021) 110920.
[8] H.M. Duvernoy, S. Delon, J. Vannson, Cortical blood vessels of the human brain, Brain Res. Bull. 7 (1981) 519–579.
[9] J. Wang, K.R. van Kranendonk, W. El-Bouri, C.B. Majoie, S.J. Payne, Mathematical modelling of haemorrhagic transformation within a multi-scale microvasculature network, Physiol Meas. (2022).
[10] W.K. El-Bouri, S.J. Payne, Investigating the effects of a penetrating vessel occlusion with a multi-scale microvasculature model of the human cerebral cortex, Neuroimage 172 (2018) 94–106.
[11] Y. Bing, D. Garcia-Gonzalez, N. Voets, A. Jérusalem, Medical imaging based in silico head model for ischaemic stroke simulation, J. Mech. Behav. Biomed. Mater. 101 (2020) 103442.
[12] J. Weickenmeier, C. Butler, P. Young, A. Goriely, E. Kuhl, The mechanics of decompressive craniectomy: personalized simulations, Comput. Methods Appl. Mech. Eng. 314 (2017) 180–195.
[13] L. Guo, J.C. Vardakis, T. Lassila, M. Mitolo, N. Ravikumar, D. Chou, M. Lange, A. Sarrami-Foroushani, B.J. Tully, Z.A. Taylor, Subject-specific multi-poroelastic model for exploring the risk factors associated with the early stages of Alzheimer's disease, Interface Focus 8 (2018) 20170019.
[14] R.M. Padmos, T.I. Józsa, W.K. El-Bouri, P.R. Konduri, S.J. Payne, A.G. Hoekstra, Coupling one-dimensional arterial blood flow to three-dimensional tissue perfusion models for in silico trials of acute ischaemic stroke, Interface Focus 11 (2021) 20190125.
[15] M.M. Mokhtarudin, S. Payne, Mathematical model of the effect of ischemia–reperfusion on brain capillary collapse and tissue swelling, Math. Biosci. 263 (2015) 111–120.
[16] X. Chen, T.I. Józsa, S.J. Payne, Computational modelling of cerebral oedema and osmotherapy following ischaemic stroke, Comput. Biol. Med. 151 (2022) 106226.
[17] T.I. Józsa, R.M. Padmos, N. Samuels, W. El-Bouri, A.G. Hoekstra, S.J. Payne, A porous circulation model of the human brain for in silico clinical trials in ischaemic stroke, Interface Focus 11 (2021) 20190127.
[18] N.E. LeCouffe, M. Kappelhof, K.M. Treurniet, L.A. Rinkel, A.E. Bruggeman, O.A. Berkhemer, L. Wolff, H. van Voorst, M.L. Tolhuisen, D.W. Dippel, A randomized trial of intravenous alteplase before endovascular treatment for stroke, N. Engl. J. Med. 385 (2021) 1833–1844.
[19] A. Jain, M. Jain, A. Kanthala, D. Damania, L. Stead, H. Wang, B. Jahromi, Association of CT perfusion parameters with hemorrhagic transformation in acute ischemic stroke, Am. J. Neuroradiol. 34 (2013) 1895–1900.
[20] W.K. El-Bouri, S.J. Payne, A statistical model of the penetrating arterioles and venules in the human cerebral cortex, Microcirculation 23 (2016) 580–590.
[21] T.W. Okell, M.A. Chappell, M.E. Kelly, P. Jezzard, Cerebral blood flow quantification using vessel-encoded arterial spin labeling, J. Cereb. Blood Flow Metab. 33 (2013) 1716–1724.
[22] H. Mutsaerts, J. Van Dalen, D. Heijtel, P. Groot, C. Majoie, E. Petersen, E. Richard, A. Nederveen, Cerebral perfusion measurements in elderly with hypertension using arterial spin labeling, PLoS One 10 (2015) e0133717.
[23] EH. Starling, On the absorption of Fluids from the Connective Tissue Spaces, J Physiol 19 (1896) 312–326.
[24] M. Mokhtarudin, Mathematical Modelling of Cerebral Ischaemia-Reperfusion Injury, University of Oxford, 2016.
[25] G. Drzewiecki, S. Field, I. Moubarak, J.K.J. Li, Vessel growth and collapsible pressure-area relationship, Am. J. Physiol. Heart Circ. Physiol. 273 (1997) H2030–H2043.
[26] M. Gliem, A.K. Mausberg, J.I. Lee, I. Simiantonakis, N. van Rooijen, H.P. Hartung, S. Jander, Macrophages prevent hemorrhagic infarct transformation in murine stroke models, Ann. Neurol. 71 (2012) 743–752.
[27] S.J. Payne, C. Lucas, Oxygen delivery from the cerebral microvasculature to tissue is governed by a single time constant of approximately 6 s, Microcirculation 25 (2018) e12428.
[28] F. Lauwers, F. Cassot, V. Lauwers-Cances, P. Puwanarajah, H. Duvernoy, Morphometry of the human cerebral cortex microcirculation: general characteristics and space-related profiles, Neuroimage 39 (2008) 936–948.
[29] M.J.M. Mokhtarudin, S.J. Payne, The study of the function of AQP4 in cerebral ischaemia–reperfusion injury using poroelastic theory, Int. J. Numer. Method Biomed. Eng. 33 (2017) e02784.
[30] B.C. Campbell, P.J. Mitchell, T.J. Kleinig, H.M. Dewey, L. Churilov, N. Yassi, B. Yan, R.J. Dowling, M.W. Parsons, T.J. Oxley, Endovascular therapy for ischemic stroke with perfusion-imaging selection, N. Engl. J. Med. 372 (2015) 1009–1018.
[31] T.G. Jovin, J.L. Saver, M. Ribo, V. Pereira, A. Furlan, A. Bonafe, B. Baxter, R. Gupta, D. Lopes, O. Jansen, Diffusion-weighted imaging or computerized tomography perfusion assessment with clinical mismatch in the triage of wake up and late presenting strokes undergoing neurointervention with Trevo (DAWN) trial methods, Int. J. Stroke 12 (2017) 641–652.
[32] S. Payne, Cerebral autoregulation: Control of Blood Flow in the Brain, Springer, 2016.
[33] B. Tully, Y. Ventikos, Cerebral water transport using multiple-network poroelastic theory: application to normal pressure hydrocephalus, J Fluid Mech 667 (2011) 188–215.
[34] S.W. Su, M. Catherall, S. Payne, The influence of network structure on the transport of blood in the human cerebral microvasculature, Microcirculation 19 (2012) 175–187.
[35] E. Lüders, H. Steinmetz, L. Jäncke, Brain size and grey matter volume in the healthy human brain, Neuroreport 13 (2002) 2371–2374.
[36] S. Payne, A model of the interaction between autoregulation and neural activation in the brain, Math. Biosci. 204 (2006) 260–281.
[37] F. Cassot, F. Lauwers, C. Fouard, S. Prohaska, V. Lauwers-Cances, A novel three-dimensional computer-assisted method for a quantitative study of microvascular networks of the human cerebral cortex, Microcirculation 13 (2006) 1–18.
[38] H. Ito, I. Kanno, H. Iida, J. Hatazawa, E. Shimosegawa, H. Tamura, T. Okudera, Arterial fraction of cerebral blood volume in humans measured by positron emission tomography, Ann. Nucl. Med. 15 (2001) 111–116.
[39] A. Logg, G.N. Wells, DOLFIN: automated finite element computing, ACM Trans. Math. Softw. (TOMS) 37 (2010) 1–28.
[40] A. Logg, K.B. Ølgaard, M.E. Rognes, G.N. Wells, in: FFC: the FEniCS Form compiler, Automated Solution of Differential Equations By the Finite Element Method, Springer, 2012, pp. 227–238.
[41] K.M. Treurniet, N.E. LeCouffe, M. Kappelhof, B.J. Emmer, A.C. van Es, J. Boiten, G.J. Lycklama, K. Keizer, L.S. Yo, H.F. Lingsma, MR CLEAN-NO IV: intravenous treatment followed by endovascular treatment versus direct endovascular treatment for acute ischemic stroke caused by a proximal intracranial occlusion—Study protocol for a randomized clinical trial, Trials 22 (2021) 1–15.

[42] N. Horie, Y. Morofuji, Y. Iki, E. Sadakata, T. Kanamoto, Y. Tateishi, T. Izumo, T. Anda, M. Morikawa, A. Tsujino, Impact of basal ganglia damage after successful endovascular recanalization for acute ischemic stroke involving lenticulostriate arteries, J. Neurosurg. 132 (2019) 1880–1888.
[43] L.R. Dice, Measures of the amount of ecologic association between species, Ecology 26 (1945) 297–302.
[44] R. Zhou, F. Guo, M.R. Azarpazhooh, J.D. Spence, E. Ukwatta, M. Ding, A. Fenster, A voxel-based fully convolution network and continuous max-flow for carotid vessel-wall-volume segmentation from 3D ultrasound images, IEEE Trans. Med. Imaging 39 (2020) 2844–2855.
[45] J.C. Griffis, J.B. Allendorfer, J.P. Szaflarski, Voxel-based Gaussian naïve Bayes classification of ischemic stroke lesions in individual T1-weighted MRI scans, J. Neurosci. Methods 257 (2016) 97–108.
[46] X. Chai, M. van Herk, M.C. Hulshof, A. Bel, A voxel-based finite element model for the prediction of bladder deformation, Med Phys 39 (2012) 55–65.
[47] T. Yamamoto, S. Kabus, J. Von Berg, C. Lorenz, M.P. Chung, J.C. Hong, B.W. Loo Jr, P.J. Keall, Reproducibility of four-dimensional computed tomography-based lung ventilation imaging, Acad. Radiol. 19 (2012) 1554–1565.
[48] J.M. Edmund, H.M. Kjer, K. Van Leemput, R.H. Hansen, J.A. Andersen, D. Andreasen, A voxel-based investigation for MRI-only radiotherapy of the brain using ultra short echo times, Phys. Med. Biol. 59 (2014) 7501.
[49] X. Papademetris, A.J. Sinusas, D.P. Dione, R.T. Constable, J.S. Duncan, Estimation of 3-D left ventricular deformation from medical images using biomechanical models, IEEE Trans. Med. Imaging 21 (2002) 786–800.
[50] Y. Çinar, A.M. Şenyol, K. Duman, Blood viscosity and blood pressure: role of temperature and hyperglycemia, Am. J. Hypertens. 14 (2001) 433–438.
[51] M. Mushtaq, M. Abdul Mateen, U.-.H. Kim, Hyperglycemia associated blood viscosity can be a nexus stimuli, Clin. Hemorheol. Microcirc. 71 (2019) 103–112.
[52] W. van der Steen, N.A. van der Ende, K.R. van Kranendonk, V. Chalos, R.J. van Oostenbrugge, W.H. van Zwam, Y.B. Roos, P.J. van Doormaal, A.C. van Es, H.F. Lingsma, Determinants of Symptomatic Intracranial Hemorrhage After Endovascular Stroke Treatment: a Retrospective Cohort Study, Stroke 53 (2022) 2818–2827.
[53] H. Bays, N. Abate, M. Chandalia, Adiposopathy: sick fat causes high blood sugar, high blood pressure and dyslipidemia, 2005, pp. 39–59.
[54] M.S. Brown, J.L. Goldstein, How LDL receptors influence cholesterol and atherosclerosis, Sci. Am. 251 (1984) 58–69.
[55] P. Libby, Atherosclerosis: the new view, Sci. Am. 286 (2002) 46–55.
[56] A.W. Armstrong, D.E. Golan, in: Pharmacology of Hemostasis and thrombosis, Principles of Pharmacology: The Pathophysiologic Basis of Drug Therapy, 3rd ed., Lippincott Williams & Wilkins, Philadelphia, 2011, pp. 372–400.
[57] A. Jenkins, W. Maxwell, D. Graham, Experimental intracerebral haematoma in the rat: sequential light microscopical changes, Neuropathol. Appl. Neurobiol. 15 (1989) 477–486.
[58] T.I. Jozsa, J. Petr, F. Barkhof, S.J. Payne, H.J. Mutsaerts, MRI-based computational model generation for cerebral perfusion simulations in health and ischaemic stroke, bioRxiv (2022) 2022-09.
[59] K.N. Vemmos, K. Spengos, G. Tsivgoulis, N. Zakopoulos, E. Manios, V. Kotsis, M. Daffertshofer, D. Vassilopoulos, Factors influencing acute blood pressure values in stroke subtypes, J. Hum. Hypertens. 18 (2004) 253–259.
[60] C. Wang, X. Chen, L. Wang, M. Makihata, H.C. Liu, T. Zhou, X. Zhao, Bioadhesive ultrasound for long-term continuous imaging of diverse organs, Science 377 (2022) 517–523.